Supporting information

Cation modulated spin state and near room temperature transition within a family of compounds containing the same $[FeL_2]^{2-}$ center

Jia-Hui Liu,[a,b] Xiao-Qing Guo,[b] Zi-Cheng Wang,[a,b] Li-Xuan Cai,[b] Li-Peng Zhou,[b] Chong-Bin Tian*[a,b] and Qing-Fu Sun*[a,b]

[a] *College of Chemistry and Materials Science, Fujian Normal University, Fuzhou 350007, China*

[b] *State Key Laboratory of Structural Chemistry, Fujian Institute of Research on the Structure of Matter, Chinese Academy of Sciences, Fuzhou 350002, China*

Email: tianchongbin@fjirsm.ac.cn, qfsun@fjirsm.ac.cn

Contents

1. Experimental procedures

1.1 General

Unless otherwise stated, all chemicals and solvents were purchased from commercial companies and used directly. Deuterated solvents were purchased from Admas, J&K scientific and Sigma-Aldrich. ^{1}H-NMR spectra were determined on a Bruker Biospin Avance III (400 MHz) spectrometer. Besides, ^{1}H-NMR chemical shifts were measured with respect to residual signals of the deuterated solvents used. ESI mass spectrometry (MS) experiments were performed on a Waters Synapt HDMS G2-Si quadrupole/time -of-flight (Q/TOF) tandem mass spectrometer. This instrument contains a triwave device between the Q and TOF analyzers, consisting of three collision cells in the order trap cell, ion mobility cell, and transfer cell. Trap and transfer cells are pressurized with Ar, and the ion mobility cell is pressurized with N_2 flowing in a direction opposite to that of the entering ions. Some MS spectra were recorded on LC-QTOF-MS from Agilent. Additionally, elemental analyses of C, H, and N were measured using a Vario EL III elemental analyzer. UV-Vis spectra are recorded on UV-2700 UV-Visible spectrophotometer from SHIMADZU. Thermogravimetric analyses were performed using a GA/NETZSCH STA449C instrument heated from 40–1000 °C (heating rate of 10 °C min^{-1}, nitrogen stream). The X-ray powder diffraction (XPRD) data were collected using Miniflex600 (Cu-Kα radiation: $\lambda = 1.54056$ Å) in the range of $5° < 2\theta < 50°$. Variable-temperature magnetic susceptibility data were collected with a Quantum Design MPMS XL superconducting quantum interference device (SQUID) magnetometer under an applied magnetic field of 1 kOe in sweep mode with a scan speed of 2 K min^{-1}. Diamagnetic corrections were made using Pascal's constants. Otherwise, TGA, elemental analyses, and variable-temperature magnetic susceptibility were performed by powder samples.

Caution! The pyridine-2,6-bi-tetrazolate-based ligands and their derivatives are potentially explosive, hence extreme care should be taken with small quantity in using and handing with them.

1.2 Syntheses and Characterization

Synthesis of self-assembled complex of H_2L:

The ligand H_2L (Pyridine-2,6-bi-tetrazolate) was synthesized by cycloaddition of sodium azide with the pyridine-2,6-dicarbonitrile in anhydrous dimethylformamide (more details see Ref S1).[1]

Synthesis of self-assembled complex 1: Adding H_2L (50.00 mg, 0.232 mmol, 1 eq.) in 100 μL DMSO, $Fe(OTf)_2$ (41.147 mg, 0.116 mmol, 0.5 eq.) and Me_4NOH (166.8 μL, 0.465 mmol, 2 eq.), to 600.0 μL DMSO and then stirred at 50 ºC for 2 h, the solution turned dark red. After cooling to room temperature, the resulting solution was exposed to slow vapor of ethyl acetate for two weeks, leading to red single crystals of **1**. When a large number of ethyl acetate was poured into the above dark red solution, red turbid liquid was formed, and then collected and washed with diethyl ether, dried in vacuum at 65 ºC for 2 h, leading to 67 mg of red powder (0.106 mmol, 91% yield based on Fe). Anal. calcd. (%) for **1** $C_{22}H_{30}FeN_{20}$ (630.51): C 41.91, N 44.43, H 4.80. Found: C 41.75, N 44.35, H 4.88. ^1H NMR (400 MHz, DMSO-*d*$_6$) δ 13.435, 7.839. ESI-TOF-MS for **1**: m/z calcd. for $[FeL_2]^{2-}$ 241.02, found 241.05; calcd. for $[FeL_2H]^-$ 483.05, found 483.08.

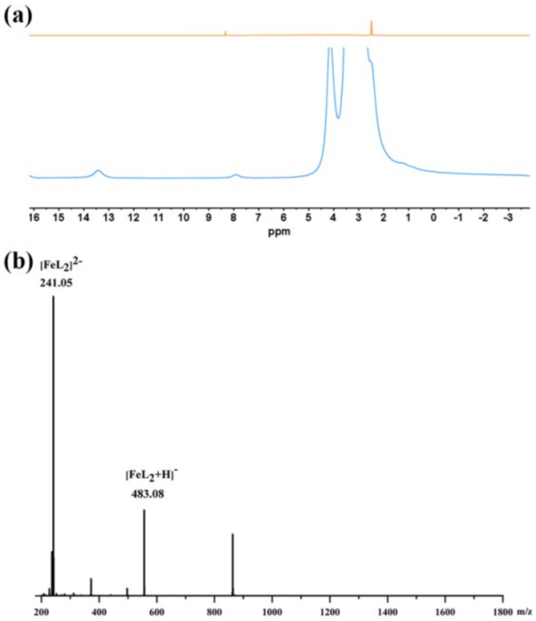

Figure S1. ^1H NMR spectrum of H_2L, **1** at 298 K. (400 MHz, *d*$_6$-DMSO) and ESI-TOF-MS spectrum of **1**.

Synthesis of self-assembled complex 2: The synthesis process was similar to **1** except that Et_2NH (48.1 μL, 0.465 mmol) was used instead of Me_4NOH. The preparation of single crystals and powder were also similar to **1**. Precipitated by ethyl acetate, giving 65 mg of orange powder (0.103 mmol, 89% yield based on Fe). Anal. calcd. (%) for **2** $C_{22}H_{30}FeN_{20}$ (630.51): C 41.91, N 44.43, H 4.80. Found: C 41.67, N 44.52, H 4.86. ^1H NMR (400 MHz, DMSO-*d*$_6$) δ 13.798, 7.952. ESI-TOF-MS for FeL_2: m/z calcd. for $[FeL_2]^{2-}$ 241.02, found 241.05; calcd. for $[FeL_2H]^-$ 483.05, found 483.08.

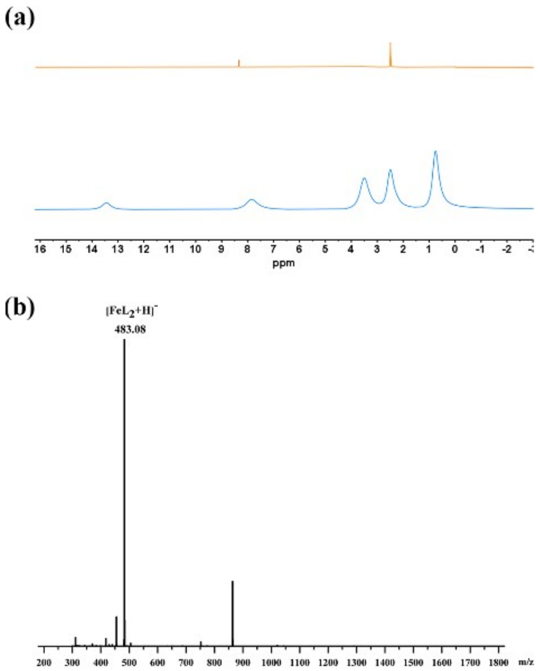

Figure S2. ^{1}H NMR spectrum of H_2L, **2** at 298 K. (400 MHz, *d*$_6$-DMSO) and ESI-TOF-MS spectrum of **2**.

Synthesis of self-assembled complex 3: The synthesis process was similar to **1** except that $^{i}Pr_2NH$ (70.7 µL, 0.465 mmol) was used instead of Me_4NOH. The preparation of single crystals and powder were also similar to **1**. Precipitated by ethyl acetate, giving 70 mg of earth-yellow powder (0.102 mmol, 88% yield based on Fe). Anal. calcd. (%) for **3** $C_{26}H_{38}FeN_{20}$ (686.61): C 45.48, N 40.80, H 5.58. Found: C 45.26, N 40.71, H 5.63. ^{1}H NMR (400 MHz, DMSO-*d*$_6$) δ 13.816, 8.039. ESI-TOF-MS for FeL_2: m/z calcd. for $[FeL_2]^{2-}$ 241.02, found 241.05; calcd. for $[FeL_2H]^-$ 483.05, found 483.08.

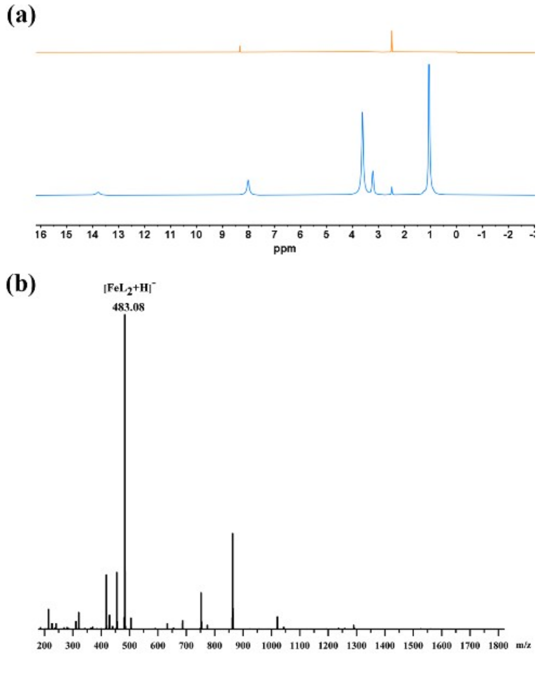

Figure S3. ^{1}H NMR spectrum of of H_2L, **3** at 298 K. (400 MHz, d_6-DMSO) and ESI-TOF-MS spectrum of **3**.

Synthesis of self-assembled complex 4: The synthesis process was similar to **1** except that ^{i}PrNH$_2$ (39.8 μL, 0.465 mmol) was used instead of Me_4NOH. The preparation of single crystals and powder were also similar to **1**. Precipitated by ethyl acetate, giving 62 mg of yellow powder (0.103 mmol, 89% yield based on Fe). Anal. calcd. (%) for **4** $C_{20}H_{26}FeN_{20}$ (602.46): C 39.87, N 46.50, H 6.36. Found: C 39.72, N 46.43, H 6.29. 1H NMR (400 MHz, DMSO-d_6) δ13.816, 7.815. ESI-TOF-MS for FeL$_2$: m/z calcd. for $[FeL_2H]^-$ 483.05, found 483.08.

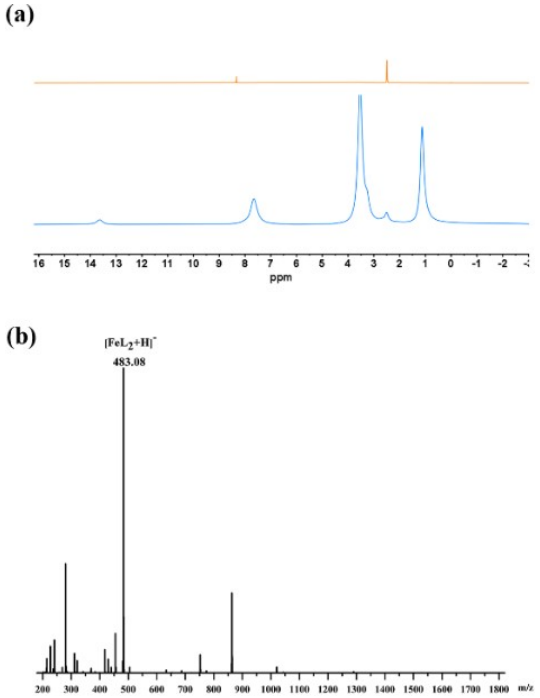

Figure S4. ^{1}H NMR spectrum of of H_2L, **4** at 298 K. (400 MHz, d_6-DMSO) and ESI-TOF-MS spectrum of **4**.

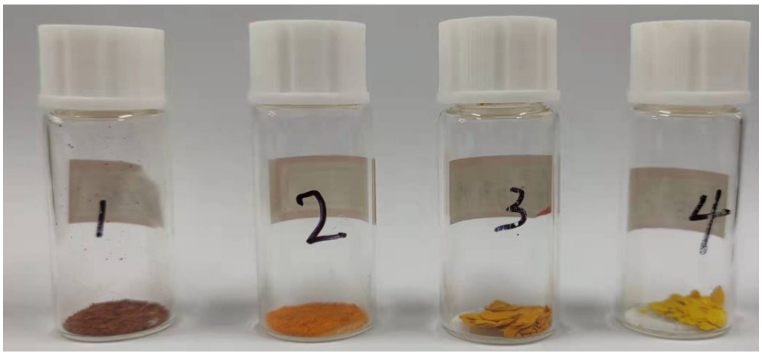

Figure S5. Color views of powder samples **1**−**4** at room temperature.

2. UV−Vis Spectroscopy

The UV–Vis spectra of complexes **1**−**4** are very similar (Figure S6), which show strong absorption in the 270–310 nm ranges, due to the $\pi \rightarrow \pi^*$ and $n \rightarrow \pi^*$ transitions on the aromatic ligands. In addition, the band at ca. 500 nm corresponds to charge transfer (CT) bands.

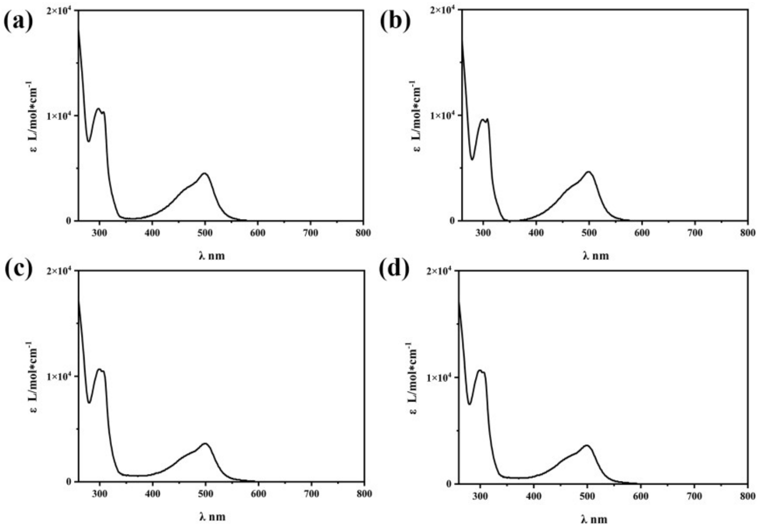

Figure S6. UV/Vis absorption spectra of **1**−**4** ($c = 1.00 \times 10^{-5}$ M in DMSO at 298 K).

3. Single crystal X-ray diffraction studies

The single crystals X-ray diffraction were carried out on micro-focus metaljet diffractometer using Ga Kα radiation (λ = 1.3405 Å). And data reduction was performed with the CrysAlisPro package,[1] at last analytical absorption correction was performed. All structures were solved by direct methods using SHELXS-97[2] and refined by full-matrix least-squares on F^2 using SHELXL-2016 program.[3] The non-hydrogen atoms were refined anisotropically for compounds **1**−**4**. Crystallographic data and other pertinent information for compounds **1**−**4**, were summarized in Table S1. Due to the presence of disorder cations in **2** at 400 K, some constraints (dfix and simu) were applied to refine the disorder cations to obtain the chemical-reasonable modes and reasonable atomic displacement parameters. CCDC numbers: 2121455 for **1** (100 K), 2121456 for **1** (400 K), 2121464 for **2** (100 K), 2121465 for **2** (400 K), 2121466 for **3** (100 K), 2121467 for **3** (298 K), 2121468 for **4** (100 K).

Table S1. Crystallographic data and structure refinement parameters for complexes **1**–**4** at different temperatures.

	1 (100 K)	**1 (400 K)**	**2 (100 K)**	**2 (400 K)**
Empirical	$C_{22}H_{30}FeN_{20}$		$C_{22}H_{30}FeN_{20}$	
Fw	630.51		630.51	
Cryst syst	Tetragonal		Monoclinic	
Space group	$I4_1/a$		$C2/c$	
a/Å	10.40180(10)	10.5565(9)	20.8907(5)	20.5868(6)
b/Å	10.40180(10)	10.5565(9)	10.0801(2)	10.3980(3)
c/Å	25.2056(3)	25.489(3)	13.7695(3)	14.0701(4)
α/°	90.00	90.00	90.00	90.00
β/°	90.00	90.00	91.482(2)	92.916(3)
γ/°	90.00	90.00	90.00	90.00
V/Å^3	2727.18(6)	2840.50(6)	2898.62(11)	3007.97(15)
Z	4	4	4	4
D_{calc}/g cm^{-3}	1.536	1.474		1.392
μ/mm^{-1}	3.36	3.23	3.16	3.05
F(000)	1312	1312	1312	1312
Parameters	102	102	197	197
R_1[a],wR_2[b] [I>2σ(I)]	0.0241/0.0634	0.0321/0.0823	0.0247/0.0674	0.0497/0.1275
R_1[a],wR_2[b] [all data]	0.0250/0.0639	0.0400/0.0854	0.0251/0.0676	0.0677/0.01371
Goodness-of-fit	1.036	1.068	1.079	1.040

Continue table

	3 (100 K)	**3 (298 K)**	**4 (100 K)**
Empirical formula	$C_{26}H_{38}FeN_{20}$		$C_{20}H_{26}FeN_{20}$
Fw	686.61		602.46
Cryst syst	Monoclinic		Monoclinic
Space group	$C2/c$		$C2/c$
a/Å	15.5423(3)	15.9965(3)	23.034(7)
b/Å	21.1135(3)	21.1381(3)	8.547(3)
c/Å	10.7801(2)	10.9355(2)	13.723(6)
α/°	90.00	90.00	90.00
β/°	107.074(2)	109.075(2)	98.673(6)
γ/°	90.00	90.00	90.00
V/Å^3	3381.60(11)	3494.65(11)	2670.7 (17)
Z	4	4	4
D_{calc}/g cm^{-3}	1.349	1.305	1.498
μ/mm^{-1}	2.74	2.65	0.62
F(000)	1440	1440	1248
Parameters	217	217	189
R_1[a],wR_2[b] [I>2σ(I)]	0.0268/0.0730	0.0278/0.0722	0.0499/0.0812
R_1[a],wR_2[b] [all data]	0.0280/0.0735	0.0301/0.0732	0.0895/0.0968
Goodness-of-fit	1.066	1.030	1.051

${}^aR_1 = \sum||F_o|-|F_c||/\sum|F_o|$, ${}^b\ wR_2 = [\sum w(F_o^2-F_c^2)^2/\sum w(F_o^2)^2]^{0.5}$.

Table S2. Selected Bond Lengths (Å) and Angles (°) for **1–4**.

1			**2**		
	100 K	400 K		100 K	400 K
Fe1−N1	1.957(1)	2.009(4)	Fe1−N1	1.985(1)	2.170(2)
Fe1−N5	1.923(1)	1.958(1)	Fe1−N5	1.942(1)	2.140(1)
N1−Fe1−N5	80.08(3)	79.13(4)	Fe1−N6	1.964(1)	2.170(2)
N1−Fe1−N1C	91.70(9)	92.04(1)	N1−Fe1−N5	79.27(5)	74.49(8)
N1−Fe1−N1D	160.16(6)	158.26(8)	N1−Fe1−N6	158.88(5)	148.75(8)
N5−Fe1−N5C	180.00	180.00	N1−Fe1−N1D	92.69(6)	94.82(11)
			N1−Fe1−N5D	103.41(5)	116.00(8)
			N1−Fe1−N6D	92.55(5)	97.50(8)
			N5−Fe1−N6	79.61(5)	74.29(8)
			N5−Fe1−N5D	176.22(6)	165.48(10)
			N5−Fe1−N6D	97.68(5)	94.98(8)
			N6−Fe1−N6D	89.89(7)	86.55(12)

Symmetry codes: For **1**: (C) y+1/4, −x+3/4, −z+3/4, (D) −x+1, −y+1/2, z; for **2**, (D) $-x+1, y, -z+3/2$;

Continue table

3			**4**	
	100 K	298 K		100 K
Fe1−N1	1.993(9)	2.197(1)	Fe1−N1	2.198(4)
Fe1−N5	1.930(1)	2.153(1)	Fe1−N5	2.169(3)
Fe1−N6	1.953(9)	2.172(10)	Fe1−N6	2.229(4)
N1−Fe1−N5	79.75(4)	74.39(4)	N1−Fe1−N5	74.25(13)
N1−Fe1−N6	159.84(4)	148.52(4)	N1−Fe1−N6	147.02(12)
N1−Fe1−N1D	94.47(5)	103.15(5)	N1−Fe1−N1E	103.03(18)
N1−Fe1−N5D	105.34(4)	115.20(4)	N1−Fe1−N5E	116.93(13)
N1−Fe1−N6D	90.59(4)	90.21(4)	N1−Fe1−N6D	89.51(13)
N5−Fe1−N6	80.10(4)	74.13(4)	N5−Fe1−N6	72.87(13)
N5−Fe1−N5D	172.69(5)	165.51(5)	N5−Fe1−N5D	163.22(19)
N5−Fe1−N6D	94.75(4)	95.73(4)	N5−Fe1−N6D	95.73(12)
N6−Fe1−N6D	91.32(5)	92.89(6)	N6−Fe1−N6D	96.32(19)

Symmetry codes: for **3**, (D) $-x+1, y, -z+1/2$; for **4**, (D) $-y+2, x, z+1/4$; (E) $y, -x+2, z-1/4$.

Table S3. The H-bonds interactions in compound **1**.

Interaction	T/K	d(D−H)/Å	d(H···A)/Å	d(D···A)/Å	∠(DHA)/°
C3−H3···N2A	100	0.95	2.43	3.36	168.70
	400	0.95	2.52	3.46	167.83
C5−H5···N4B	100	0.98	2.35	3.31	167.03
	400	0.98	2.36	3.33	170.29

Symmetric codes: (A) y−1/4, −x+3/4, z−1/4, (B) −y+3/4, x+1/4, z+1/4.

Table S4. Intermolecular π-π interactions of compounds **1**, **2**, **3** and **4** at lower and higher temperature.

	1		**2**		**3**		**4**
T(K)	100	400	100	400	100	298	100
π-π (d_{plane}/Å)	3.47	3.55	3.38	3.43	3.22	3.38	3.28

Table S5. The H-bonds interactions in compound **2**.

Interaction	T/K	d(D−H)/Å	d(H···A)/Å	d(D···A)/Å	∠(DHA)/°
N10−H1···N8	100	0.91	1.88	2.79	178.08
	400	0.91	1.90	2.81	176.70
N10−H2···N3A	100	0.91	1.96	2.86	171.71
	400	0.91	1.98	2.89	177.64
C3−H3···N2B	100	0.95	2.55	3.43	153.80
	400	0.95	2.70	3.45	141.96
C10−H12···N7C	100	0.99	2.63	3.56	155.51
	400	0.99	2.61	3.44	139.38

Asymmetric codes: (A) −x+1, y+1, −z+3/2; (B) x, −y, z−1/2; (C) −x+3/2, y+1/2, −z+3/2.

Table S6. The H-bonds interactions in compound **3**.

Interaction	T/K	d(D−H)/Å	d(H···A)/Å	d(D···A)/Å	∠(DHA)/°
N10−H1···N3A	100	0.89	1.99	2.88	178.11
	400	0.89	2.00	2.89	176.74
N10−H2···N8	100	0.89	1.98	2.87	174.59
	400	0.89	1.98	2.87	175.77
C3−H3···N2B	100	0.93	2.64	3.31	128.92
	400	0.93	2.74	3.45	133.46
C9−H9···N9C	100	0.98	2.54	3.34	138.59
	400	0.98	2.67	3.48	139.92
C12−H15···N4A	100	0.96	2.62	3.50	152.79

	400	0.96	2.70	3.59	154.44

Asymmetric codes: (A) x+1/2, −y+1/2, z−1/2; (B) x+1/2, −y+1/2, z+1/2; (C) x, −y+1, z−1/2.

Table S7. The H-bonds interactions in compound **4**.

Interaction	T/K	d(D−H)/Å	d(H···A)/Å	d(D···A)/Å	∠(DHA)/°
N10−H10···N7	100	0.91	1.96	2.85	164.68
N10−H11···N3A	100	0.91	2.05	2.88	151.43
N10−H12···N9B	100	0.91	1.99	2.90	172.00
C3−H3···N2C	100	0.95	2.53	3.19	126.94
C10−H15···N8D	100	0.98	3.01	3.83	142.79

Asymmetric codes: (A) −x+1, y−1, −z+3/2; (B) x, −y, z+1/2; (C) x, −y+1, z−1/2; (D) −x+1/2, y−1/2, −z+3/2.

Table S8. The NH···N H-bonds distances (D···A) in compounds **2−4** at 100 K.

	Interaction	d(D···A)/Å
Compound **2**	N10−H1···N8	2.79
	N10−H2···N3#	2.86
Compound **3**	N10−H1···N3#	2.88
	N10−H2···N8	2.87
Compound **4**	N10−H10···N7	2.85
	N10−H11···N3#	2.88
	N10−H12···N9#	2.90

represents the asymmetric codes and was not shown here for clarity.

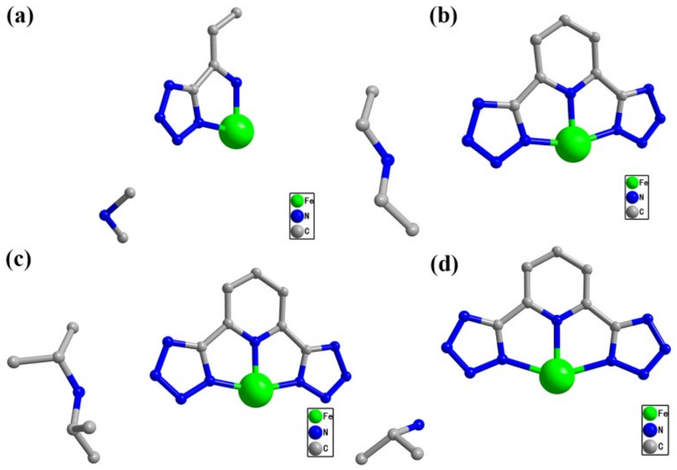

Figure S7. The asymmetric unit compounds **1** (a), **2** (b), **3** (c) and **4** (d) at 100 K. Hydrogen atoms are omitted for clarity.

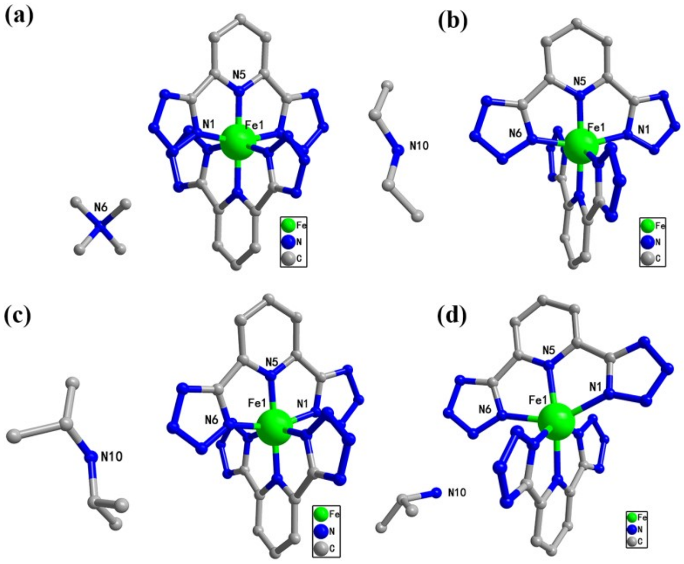

Figure S8. The coordination environment of Fe^{II} ions in compounds **1** (a), **2** (b), **3** (c) and **4** (d) at 100 K. Hydrogen atoms are omitted for clarity.

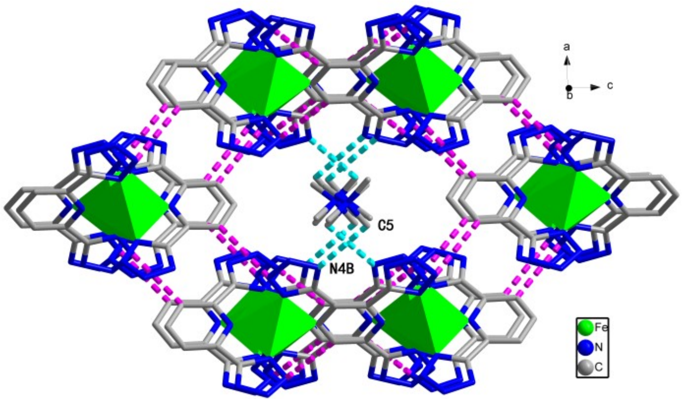

Figure S9. View of the supramolecular structure of **1** showing the Me_4N^+ cations in the cavities.

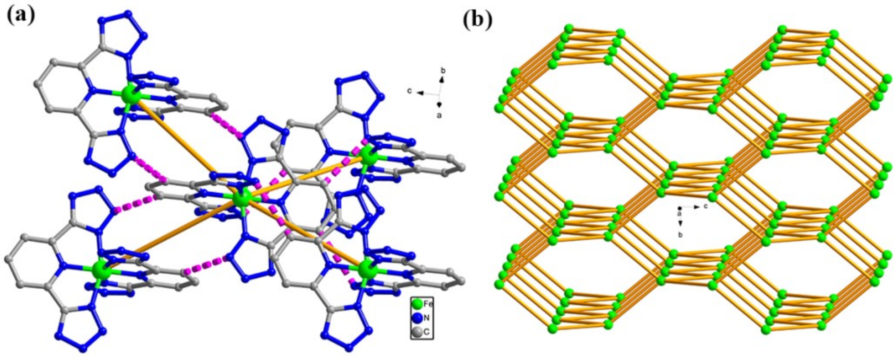

Figure S10. (a) View of topological simplification mode of compound **1**. (b) The four-connected dia topological anionic network of compound **1**.

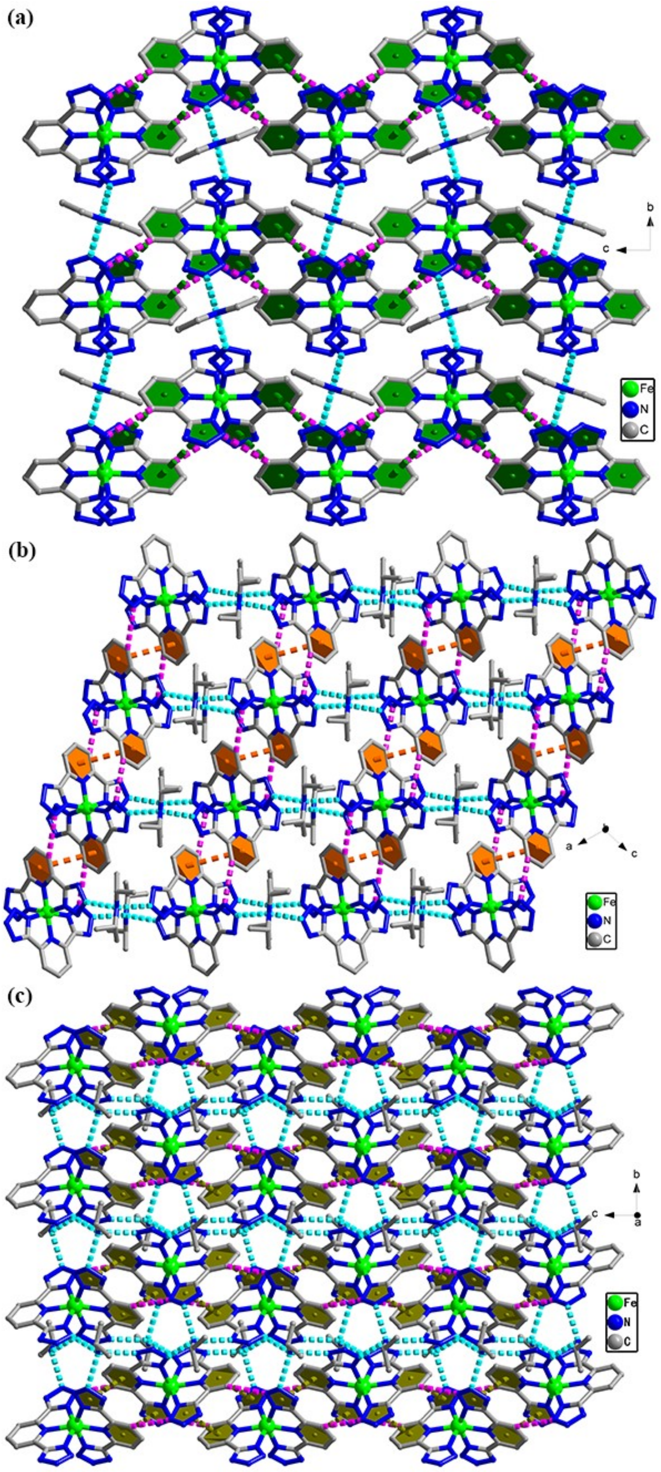

Figure S11. View of 2D supramolecular layer structure of compound **2** at 100 K (a), **3** at 100 K (b), and **4** at 100 K (c), fabricated by intermolecular C−H···N (pink dotted lines for **2**−**4**) and N−H···N (turquoise dotted lines for **2**−**4**) H-bonds interactions and π−π interactions (green, orange and dark yellow dotted lines for **2**, **3** and **4**, respectively).

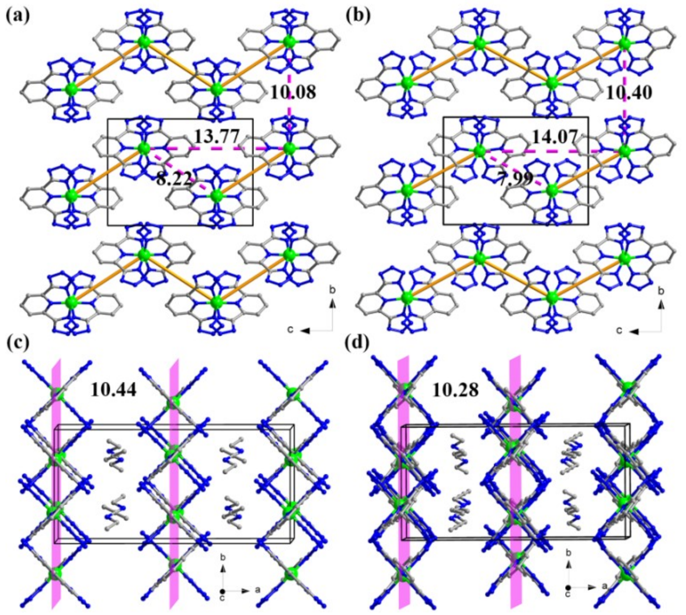

Figure S12. View of intra-chain and inter-chain Fe−Fe distances at 100 K (a) and 400 K (b) for **2**, view of interlayer distances at 100 K (c) and 400 K (d) for **2**. The unit cell edges are shown as solid black line. The light orange solid lines represent the zigzag like chain.

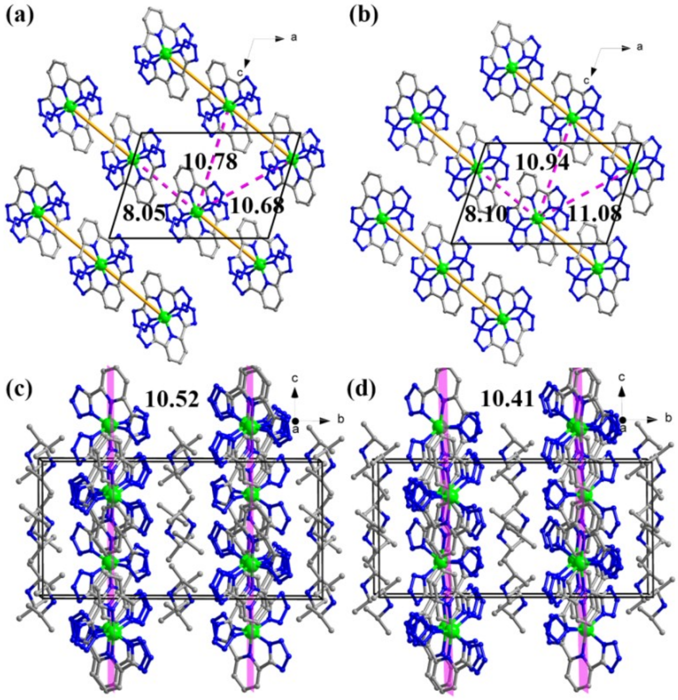

Figure S13. View of intra-chain and inter-chain Fe−Fe distance at 100 K (a) and 298 K (b) for **3**, view of interlayer distance at 100 K (c) and 298 K (d) for **3**. The unit cell edges are shown as solid black line. The light orange solid lines represent the linear chain.

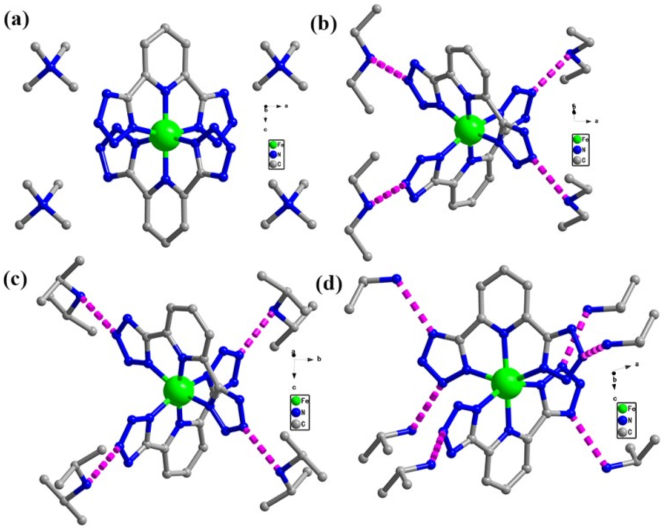

Figure S14. The number of inter-ions N−H···N H-bonds around the anionic $[Fe(L)_2]^{2-}$ center in compounds **1**−**4** at 100 K, zero for **1** (a), four for **2** (b) and **3** (c), six for **4** (d).

4. Variable-temperature magnetic susceptibility and hirshfeld Analysis

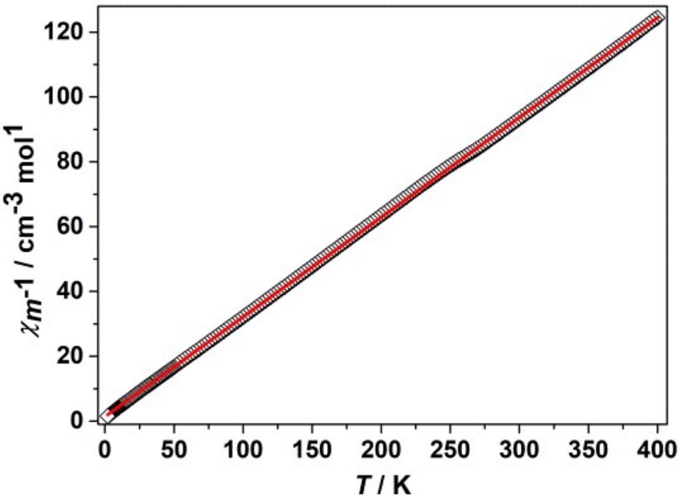

Figure S15. The curve of $1/x_m - T$ for **4**. The red line represents the best fitting with Curie-Weiss law in the corresponding temperature range.

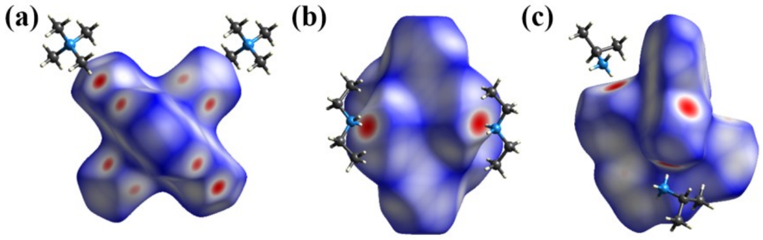

Figure S16. Hirshfeld surfaces with the strongest intermolecular contacts (in red area on the surfaces) between cation and $[Fe(L)_2]^{2-}$ molecules for **1** (a), **2** (b) and **4** (c)

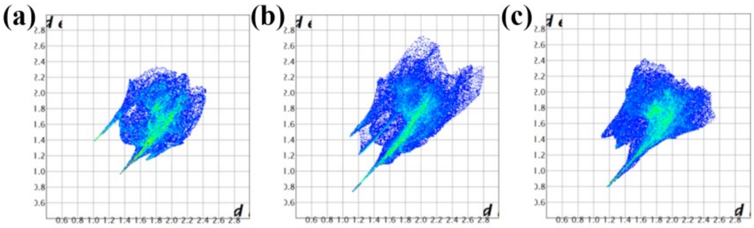

Figure S17. 2D fingerprint plots for **1** (a), **2** (b) and **4** (c).

5. Thermogravimetric analyses (TGA)

To investigate the thermal stability of compounds **1**−**4**, thermogravimetric analyses (TGA) have been performed on powder samples in a N_2 atmosphere at a heating rate of 10 ºC min^{-1} (Figure S40). The TGA curves remain nearly unchanged up to 170 °C, 170 °C, 167 °C and 230 °C, for compounds **1**−**4**, respectively, which indicates the thermal stabilities of compounds **1**−**4** can reach at least 167 °C (440 K). The TGA analyses mean that the decomposition of the titled compounds don't occur in the temperature range of magnetic measurement (2−400 K), and also the absence of solvent molecules.

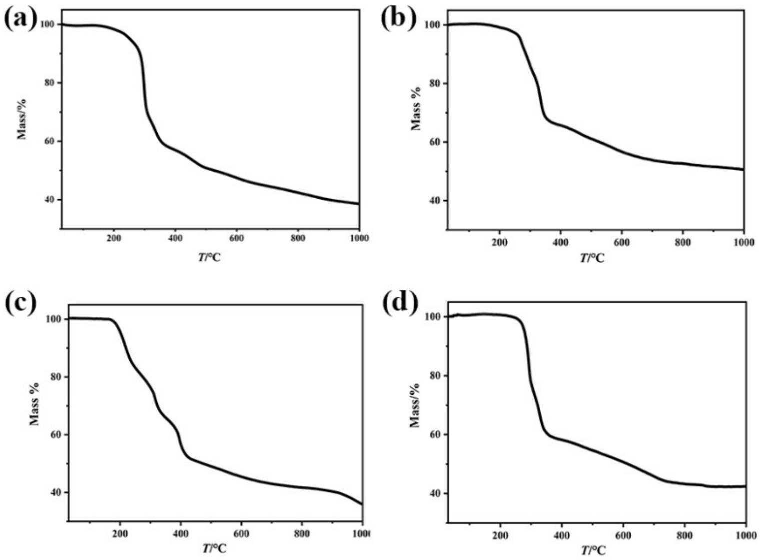

Figure S18. TGA profiles for compounds **1** (a), **2** (b), **3** (c) and **4** (d).

6. X-ray Powder diffraction data

The measured PXRD patterns of **1**−**4** are matched well with the simulated patterns generated from the results of single crystal X-ray diffraction data, indicating phase purity of the as-synthesized powder sample.

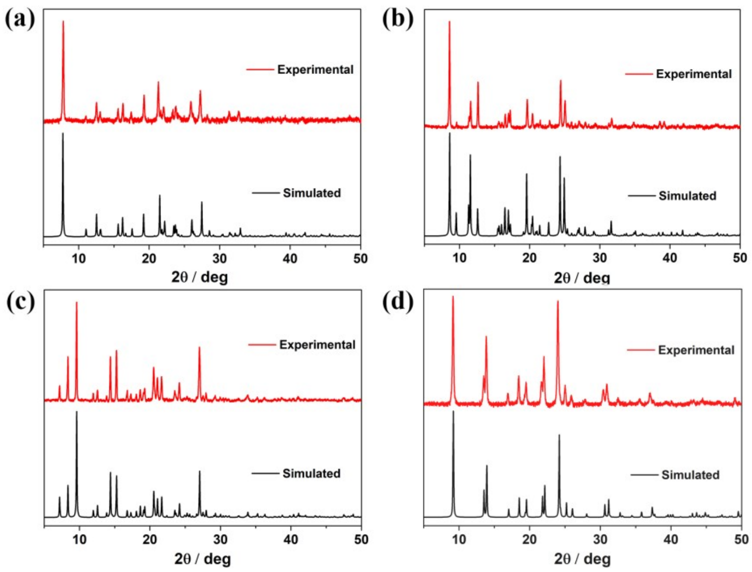

Figure S19. The X-ray powder diffraction data for compounds **1** (a), **2** (b), **3** (c) and **4** (d). The simulated data are obtained from the results of single crystal X-ray diffraction data at 400 K, 400 K, 298 K and 100 K, for **1**−**4**, respectively.

7. References

1. E. S. Andreiadis, D. Imbert, J. Pecaut, R. Demadrille, M. Mazzanti, Self-assembly of highly luminescent lanthanide complexes promoted by pyridine-tetrazolate ligands. *Dalton Trans.* 2012**, 41**, 1268-1277.
2. Agilent Technologies, *CrysAlisPro v.* 1.171.36.28, **2013**.
3. G. M. Sheldrick, SHELXL-97, Program for X-ray Crystal Structure Refinement.; University of Göttingen, Germany. **1997**.
4. G. M. Sheldrick, Crystal structure refinement with SHELXL. *Acta Crystallogr. Sec. C: Struct. Chem.* 2015**, 71**, 3-8.